Local inversion of magnetic anomalies: Implication for Mars' crustal evolution

Yoann Quesnel, Benoit Langlais, Christophe Sotin

Local inversion of magnetic anomalies: Implication for Mars' crustal evolution

Yoann Quesnel, Benoit Langlais, Christophe Sotin

Université de Nantes, Nantes Atlantique Universités, CNRS, Laboratoire de Planétologie et Géodynamique, UMR 6112, Faculté des Sciences et des Techniques, 2, rue de la Houssinière, BP 92205, Nantes, F-44000, France

Abstract

Martian magnetic anomalies have been revealed by the Mars Global Surveyor (MGS) mission in the south hemisphere of Mars. The present study models anomalies located in the ancient Terra Sirenum area between latitudes 26°S and 40°S and longitudes 185°E and 210°E using forward and inverse approaches. While the high-altitude measurements reveal the presence of two main magnetic anomalies, three are detected by low-altitude data. They are modeled as uncorrelated dipolar sources. Forward models predict large magnetizations between 30 and 60 A/m. A generalized non-linear inversion is used to determine the characteristics of the dipoles, based on different subsets of data. Low-altitude measurements inversion leads to more reliable results than those obtained by the inversion of high-altitude measurements only. Inversion of both low- and high-altitude data together provides with three dipoles that explain more than 57% of the signal, within this 10^6 km^2 area. All dipoles have large magnetizations. Serpentinization of the early martian crust can explain such remanent magnetizations. Two resulting dipoles are 56 km deep, which suggests a locally thick martian crust. The last one is shallower (31 km). This indicates different origins and/or magnetization processes. Paleomagnetic poles are calculated and located around the Tharsis bulge. It suggests that Tharsis formed at high latitudes and moved toward its present location by polar reorientation.

Keywords: Mars; Magnetic field; Lithospheric sources; Local inversion; Polar wander

1. Introduction

The MAG/ER experiment onboard the Mars Global Surveyor (MGS) spacecraft detected strong and localized magnetic anomalies on Mars (Acuña et al., 1999). No Earth-like global magnetic field was measured. Instead, there is a strong lithospheric field of remanent origin. It indicates that an intense global magnetic field was present at some time in the past. The nature of the processes that led to the formation of these magnetic anomalies is still debated. One possibility is that the magnetic field was recorded by Fe-bearing minerals contained in the crust as they cooled down below their Curie temperature, either during the accretion or later. Hydrothermal activity has also been proposed as a source of magnetization (Scott and Fuller, 2004), based on the spatial coherence between strong magnetic anomalies and valley networks (Jakosky and Phillips, 2001; Harrison and Grimm, 2002; Hood et al., 2005). Understanding the origin and timing of these magnetic anomalies would provide strong constraints on Mars' thermal history and on the evolution of its water cycle if one can prove that hydrothermal activity is responsible for their formation.

Several studies have been made to derive global constant-altitude maps of the remanent magnetic field. Terrestrial methods were used such as spherical harmonics analysis (Cain et al., 2003; Arkani-Hamed, 2004). This method provides a global view of the magnetic field of Mars. Equivalent source dipole methods were also used (Purucker et al., 2000; Langlais et al., 2004), which give further information on what could be the magnetization.

Other studies dealt with isolated anomalies. Some are based on the Mapping Orbit phase dataset (~400 km altitude). Smrekar et al. (2004) focused on a small area of the crustal dichotomy (50–90°E). Using gravity and magnetic forward modeling methods, they tested several magnetization intensities and inclinations. 10 km-thick bodies associated with a 150 kg/m^3 density contrast, a 9 A/m magnetization intensity and a 30° inclination are used to fit the gravity and magnetic signals. Frawley and Taylor (2004) also performed forward modeling and inversion of several isolated magnetic anomalies. Depths to the sources range between 0 and 160 km, depending on the anomaly. These high-altitude data however do not allow magnetic signatures and surface structures to be correlated on a very local scale. Lower altitude (100–300 km) AeroBraking phase (AB) and Science Phasing Orbit (SPO) measurements were also used. Arkani-Hamed (2001) used vertical prisms with circular cross-sections to model four isolated 120 km altitude magnetic anomalies. A 5 A/m magnetization contrast between these bodies and the surrounding crust was found.

These two high and low-altitude datasets are highly complementary. While the MO measurements provide us with a global view of the magnetic anomalies, the smaller wavelengths present in the AB dataset allow local studies to be performed. Here we propose to use together AB and MO measurements in a generalized non-linear inversion scheme to derive characteristics of local magnetic sources. We consider an area located within Terra Sirenum, between latitude 26°S and 40°S, longitude 185°E and 210°E (Fig. 1). Its age is Noachian (Tanaka, 1986; Hartmann and Neukum, 2001). The mean surface elevation is 1.5 km but large variations exist from the base of Newton impact crater (−2.3 km) to the top of a plateau located in the center of the region (4 km). Crater diameters range from less than 1 to almost 300 km for Newton. There is also a long thin ENE-WSW transverse fault (Sirenum Fossae). This may be the manifestation of a subsurface dike emplacement (Wilson and Head, 2002), or a fault correlated with the Tharsis dome emplacement during the middle- to late- Noachian (Solomon et al., 2005). A strong negative free-air gravity signature correlates with the Newton crater (−183 mgal based on the model of Yuan et al., 2001). Although the resolution of the gravity model prevents any conclusion about isostatic compensation for the other smaller craters, the compensation percentage for Newton (57% for a crustal density of 3000 kg/m^3) suggests that its emplacement occurred in a cold and rigid lithosphere, and that smaller craters in this area are not compensated.

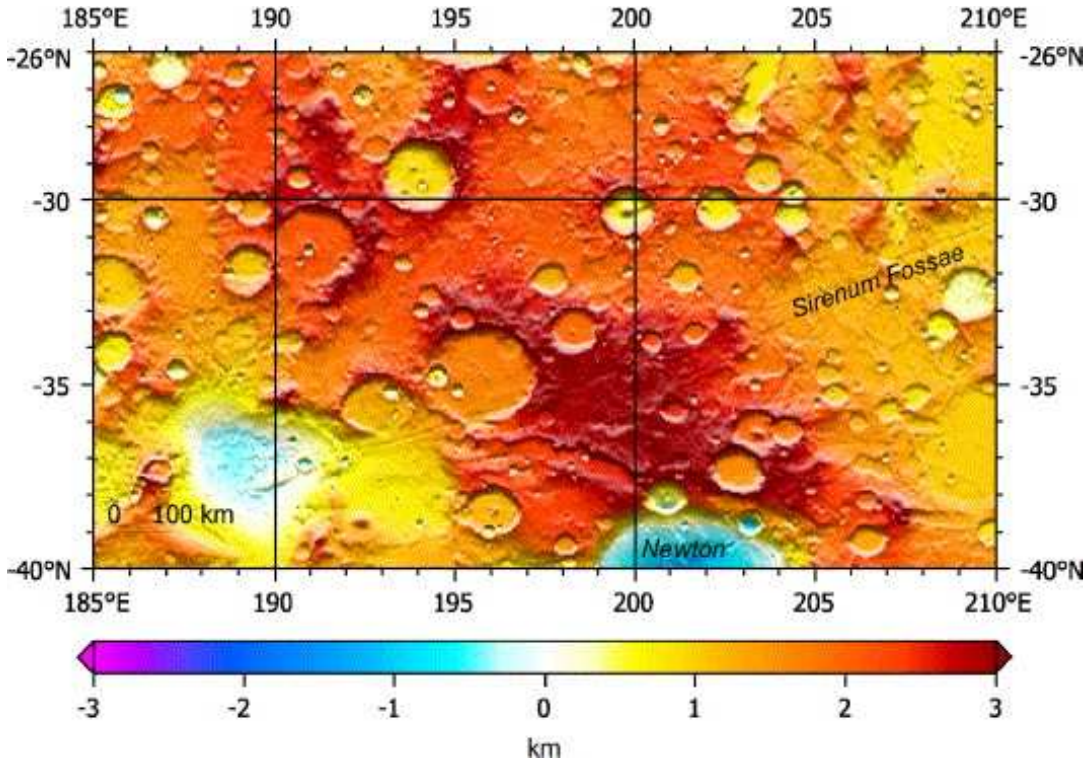

Figure 1: Topography of the studied area.

The paper is constructed in the following way. In the first part, we present the dataset used. The inversion of the magnetic data is based on the theory of nonlinear generalized inversion described by Tarantola and Valette (1982). The application to the magnetic data sets is described in the second part of the paper. Then the results in terms of depth of the anomalies and magnetization of the magnetic sources are described. Finally, we discuss the possible geological processes responsible for the crustal magnetization and the thermal evolution of the martian crust in this area.

2. Data processing and inversion scheme

2.1. Data description

During the MGS mission, magnetic data were obtained during AeroBraking (AB) phase and Mapping Orbit (MO) phase. AB measurements under 250 km altitude are considered. These data were mostly acquired on the dayside of Mars. Errors due to possible external fields are counterbalanced by the low altitude and thus the better sensitivity of the measurements to close-to-the-surface magnetic sources. MO nightside measurements are used to better constrain the large scale magnetic field. The inversion process uses magnetic data along track at a ~1 Hz sampling rate. The three components of the magnetic field are taken into account. B_r is the radial component (positive outward), B_θ the north-south component (positive southward) and B_ϕ the east–west component (positive eastward). More weight is given to the radial component, because it is less contaminated by external fields.

Measurements are shown above the region of interest in Fig. 2. In this area, altitude ranges between 102 and 250 km for AB measurements, and between 364 and 377 km for MO. Altitude of adjacent AB tracks can differ a lot. Due to orbital parameters, altitude of MO measurements at a given

latitude remains almost constant. The AB B_r component shows a very strong positive magnetic extrema centered near (32°S, 191°E). It is denoted anomaly AB-A in the rest of the paper. A 120 km diameter crater is located one degree North of the peak of anomaly AB-A. Two other anomalies (denoted AB-B and AB-C) located at (35°S, 199°E) and (32°S, 204°E) show up at this altitude. The MO B_r data map shows that the coverage is almost complete. A large and smooth positive anomaly is located at (33°S, 191°E). It seems correlated with anomaly AB-A. This anomaly is denoted MO-A. A negative anomaly shows up in the radial component in the East but not clearly in the total magnetic field. This second anomaly corresponds to the anomaly AB-C although it seems to be located more to the East. It is denoted anomaly MO-C.

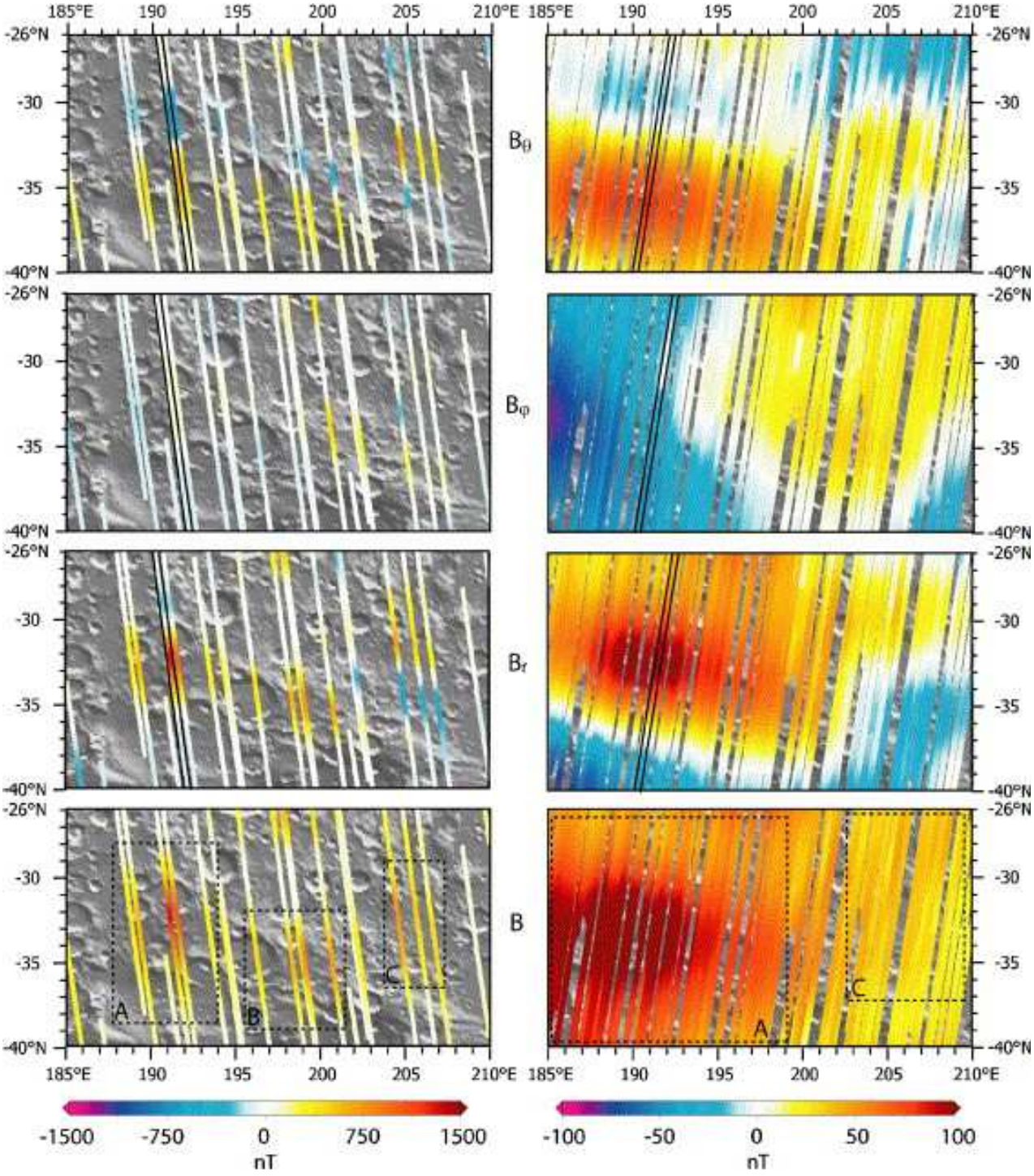

Figure 2: MGS MAG/ER AB (left) and MO (right) magnetic field measurements in the studied area. Dashed squares limit the different subsets of data for the inversions of AB-A, -B and -C anomalies on the AB B component map, and MO-A and -C on the MO B component map. Profiles with black borders are selected to represent AB-A and MO-A anomaly (see Fig. 3).

From these simple observations, it seems that the source of anomaly AB- and MO-A is deeper and stronger than the ones of anomaly AB-B, AB- and MO-C. One purpose of the inversion will be to compare how these anomalies are consistent with the two data sets and to compare separate inversion to global inversion of both data sets.

2.2. Forward models

Outside the sources, the magnetic field $\vec{B}$ is expressed as the gradient of a magnetic potential V:

$$\vec{B} = -\vec{\nabla} V \quad (1)$$

On a point P at a distance r from the dipole of moment m, this potential V is expressed as:

$$V(P) = C_m \frac{\vec{m} \cdot \vec{r}}{r^3} \quad (2)$$

where C_m is a constant (10^{-7} S.I.) (e.g. Blakely, 1995). The resulting magnetic field created by a uniformly magnetized sphere of dipolar moment $\vec{m}$ is expressed as:

$$B_x = \frac{C_m}{r^5}[3(m_x \cdot r_x + m_y \cdot r_y + m_z \cdot r_z) \cdot r_x - (r_x^2 + r_y^2 + r_z^2) \cdot m_x] = -B_\theta \quad , (3a)$$

$$B_y = \frac{C_m}{r^5}[3(m_x \cdot r_x + m_y \cdot r_y + m_z \cdot r_z) \cdot r_y - (r_x^2 + r_y^2 + r_z^2) \cdot m_y] = B_\varphi \quad , (3b)$$

$$B_z = \frac{C_m}{r^5}[3(m_x \cdot r_x + m_y \cdot r_y + m_z \cdot r_z) \cdot r_z - (r_x^2 + r_y^2 + r_z^2) \cdot m_z] = -B_r \quad , (3c)$$

where (m_x, m_y, m_z) and (r_x, r_y, r_z) are the components of $\vec{m}$ and $\vec{r}$, respectively. The dipolar moment $\vec{m}$ is the product of the magnetization by the volume of the sphere. Such a geometry can easily be associated with a geological setting.

Uniformly magnetized prisms are also used. Such prisms can be interpreted as dikes for instance. This is based on the equations of Plouff (1976):

$B_x = M_x \cdot V_1 + M_y \cdot V_2 + M_z \cdot V_3 = -B_\theta$, (4a)
$B_y = M_x \cdot V_2 + M_y \cdot V_4 + M_z \cdot V_5 = B_\phi$, (4b)
$B_y = M_x \cdot V_2 + M_y \cdot V_4 + M_z \cdot V_5 = B_\phi$, (4c)

where M_x, M_y and M_z are the three components of the magnetization vector, and V_{1-6} are volume integrals defined by Talwani (1965).

These forward models give an idea of the sources responsible for the magnetic anomalies. They also serve as inputs in the following inverse problem.

2.3. Inverse models

The equations to be solved are those of the uniformly magnetized sphere, equivalent to a dipole. The problem is nonlinear due to the intrinsic dependance of Eqs. (3a), (3a) and (3c) with the six parameters m_x, m_y, m_z, r_x, r_y and r_z. Forward models are used to estimate reasonable *a priori* values of these parameters.

Tarantola and Valette (1982) described the theory of generalized nonlinear inversion. The algorithm used in our study is based on their Eq. (24):

$$p_{k+1} = p_0 + (G_k^T \cdot C_{d_0 d_0}^{-1} \cdot G_k + C_{p_0 p_0}^{-1})^{-1} \cdot G_k^T \cdot C_{d_0 d_0}^{-1} \cdot [d_0 - g(p_k) + G_k \cdot (p_k - p_0)] \quad , (5)$$

where p_{k+1} is the parameter vector at the iteration (k+1) and p_0 is the *a priori* parameter vector. d_0 is the data vector, and $g(p_k)$ is the predicted data vector at the iteration k. G_k is the matrix of partial derivatives ($G_k = \partial g / \partial p_k$) at the iteration k. C_{d0d0} and C_{p0p0} are, respectively, the covariance matrix of data and *a priori* parameters. Data and initial parameters are assigned to small and large Standard Deviations (SD), respectively.

The algorithm is iterative. At each step χ^2 is computed:

$$\chi^2 = \frac{\Sigma_{k=1}^{N} ((g(p_k) - d_0) / (C_{d_0 d_0})^{1/2})^2}{N} \quad , (6)$$

with N, the number of measurements. The inversion runs for a large number of iterations. The model associated with a closest-to-unity χ^2 is kept. This avoids iterations stopping at a local minimum. Input parameters, data, and SDs may be adjusted in order to obtain a nearest-to-unity value of the best χ^2. *A posteriori* tests on misfits are applied to verify their final gaussian distribution. Possible outliers are then removed and a new inversion is performed.

3. Results

Results of forward modeling are first introduced. These results serve as input parameters for the inversion using either AB, MO, or AB+MO datasets.

3.1. Forward modeling

The three AB-A, AB-B, and AB-C magnetic anomalies are modelled using three uniformly magnetized spheres. The center of each sphere is located beneath the maximum of the total magnetic field. Source depth and magnetization influence the amplitude of the signal. The shape of a given anomaly is first adjusted by the inclination I and the declination D, and then by moving the location of the center of the source. Parameters of the spheres are indicated in Table 1. The predicted field associated with anomaly AB-A along a AB track is shown in Fig. 3a (the orbit passes above the AB-A magnetic source; see Fig. 2). The low-altitude observations are well fitted by the model. Root mean square (rms) residuals between measurements and predictions for anomaly A dataset are 98, 112 and 77 nT for B_r, B_θ and B_ϕ, respectively (rms measurements are 353, 278 and 96 nT, respectively). Correlation coefficients are 0.95, 0.98 and 0.75. The poorer fit of B_ϕ may be explained by larger external field in this component. Predictions for high-altitude measurements are weaker, as shown on Fig. 3b (the corresponding profile is shown in Fig. 2). Associated correlation coefficients are 0.47, 0.91, 0.89, but rms residuals are large (~33 nT) compared to the measurements (~42 nT). Similar observations are made for AB-B and AB-C anomalies. Although

the anomalies are close to each other, their sources have not necessarily the same characteristics, except for a large depth and a strong magnetization. The AB-A and AB-B sources have a steep inclination, while the AB-C one is horizontal.

Table 1. Spheres forward model parameters for AB anomalies

Anomaly	**Lat. (°N)**	**Lon. (°E)**	**Depth (km)**	***m*** **(10^{16} A m^2)**	***I*** **(°)**	***D*** **(°)**
AB-A	−32.0	191.0	50	2.7	−60	180
AB-B	−35.0	199.0	50	1.7	−50	70
AB-C	−32.8	204.0	60	3.4	0	0

Each sphere is assumed to be tangent to the surface. Corresponding magnetization intensity values are 51.6, 32.5 and 37.6 A/m, for AB-A, -B and -C spheres, respectively.

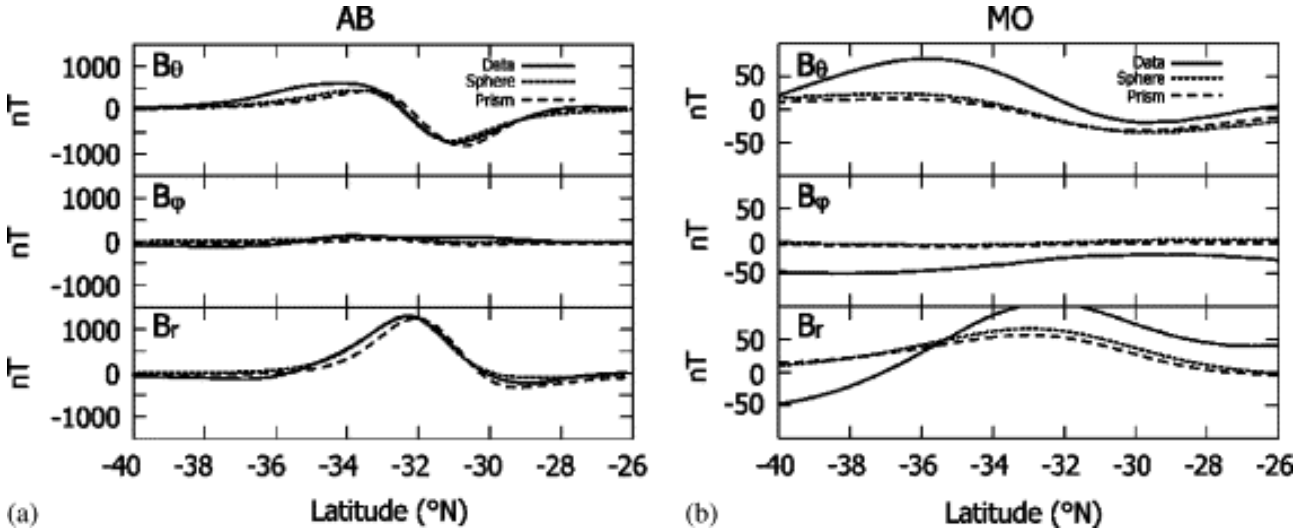

Figure 3: AB (a) and MO (b) profiles comparison between data (solid line) and forward models (dashed line), for anomaly AB-A and MO-A. The selected profiles are shown with black borders in Fig. 2. The parameters of the forward models are shown in Table 1 and Table 2.

Uniformly magnetized prisms are also investigated. There are more parameters than uniformly magnetized spheres. Notably, lateral dimensions influence the signal. Several configurations are then tested. Resulting parameters are given in Table 2. The field associated with AB-A source along a AB track is also shown on Fig. 3a. AB-A field predictions are not as good as those of uniformly magnetized spheres (124, 133 and 72 nT for B_r, B_θ and B_ϕ rms residuals). Again, the high-altitude measurements are not well predicted (Fig. 3b; B_r, B_θ and B_ϕ rms residuals are 43, 36 and 31 nT). Source parameters are very close to each other (sphere vs. prism). The only noticeable difference arises for AB-B anomaly; this may be related to the weaker amplitude of this anomaly, which makes it more difficult to characterize. Despite the simplicity of these approaches, they both lead to a similar conclusion. There is a significant magnetization associated with these anomalies.

Table 2. Prisms forward model parameters for AB anomalies

Anomaly	Lat. 1 (°N)	Lat. 2 (°N)	Lon. 1 (°E)	Lon. 2 (°E)	Thickness (km)	m (10^{16} A m^2)	I (°)	D (°)
AB-A	−32.5	−30.5	190	192	50	2.1	−40	180
AB-B	−35.5	−33.5	198	200	25	1.0	−65	180
AB-C	−33.3	−32.3	203	205	60	2.1	5	10

Lat. 1, Lat. 2, Lon. 1 and Lon. 2 correspond to South, North, West and East limits of the prisms, respectively. Each prism has its roof at the surface. Corresponding magnetization intensity values are 35.3, 34.8 and 59.7 A/m, for AB-A, -B and -C prisms, respectively.

3.2. Inversion of low-altitude anomalies

In the following, we use the forward modeling results as input parameters for the inverse problem. We first consider three subsets of the AB dataset separately, one for each AB anomaly. Their limits are shown in Fig. 2. The three subsets contain 299, 179 and 150 vector triplets, respectively. Then, all three subsets are used together. Finally, all AB measurements are taken into account.

Initial data SDs are set to 30% of the measured magnetic field, but are never lower than 75 nT. Initial SD on each component of the magnetization is set to 200%, in order to allow for a large parameter space exploration. The initial value of dipolar moment is 10^{16} A.m^2. The location of the dipole is less constrained perpendicularly to the N–S direction of the tracks. Therefore the SD on latitude is larger than the one on longitude (100 km vs. 1 km). In other words, the anomaly is imposed to lie beneath the tracks. Larger SDs on longitude would have resulted in dipoles away from the track area.

Single altitude measurements weakly constrain the source depths. As a consequence, a systematic exploration for initial values of the latter is made. We also observe that the final depth and the dipolar moment strongly depend on each other. The deeper the source, the larger the dipolar moment. Fig. 4 shows the evolution of χ^2 (Eq. (6)) as a function of the initial depth for anomaly AB-A inversion. A minimum is reached for an initial depth of 50 km (which yields a final value of 49 km). This is the value we use, with a SD set to 10 km. The same procedure is applied for anomalies AB-B and AB-C.

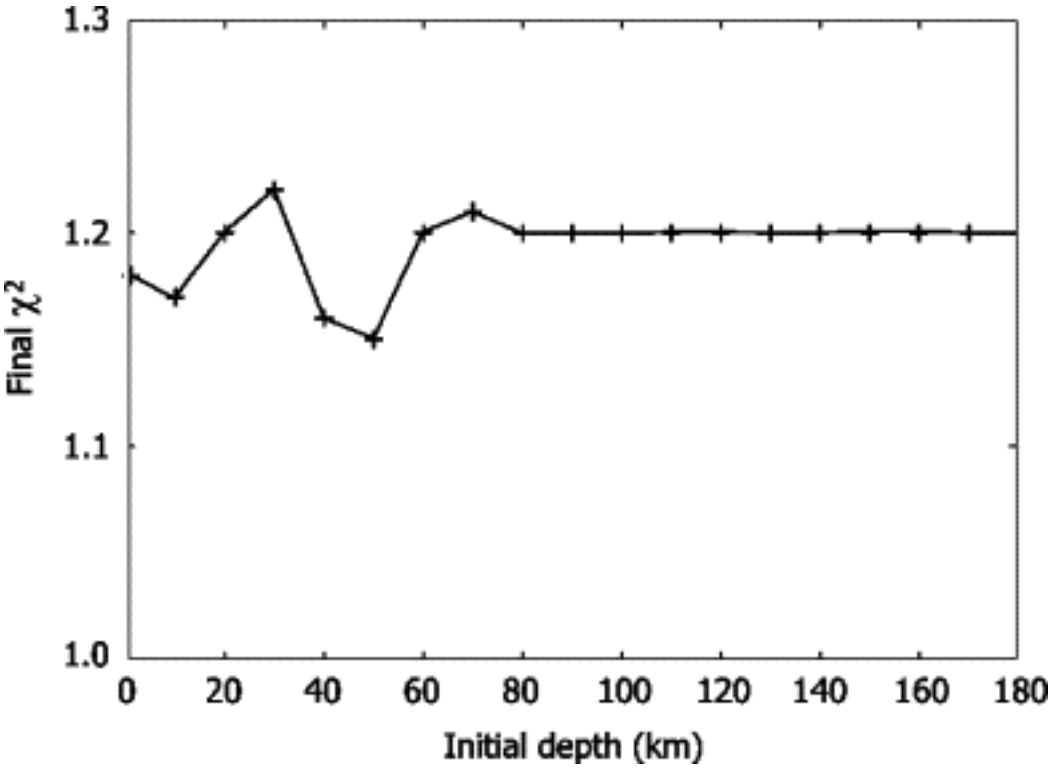

Figure 4: Final chi-squared dependance with initial depth for inversion AB-A.

The input and resulting parameters for the AB-A dipole are shown in Table 3. There is a rapid convergence toward a stable solution after a few iterations. The final distribution of data misfits approaches a gaussian one, but the peak is shifted. Final parameter SDs are small compared to the initial one. SD of the dipolar moment falls off during the inversion (87% of the value to 2.7%). The same observation is made for the depth (20%–0.9%). The solution appears to be a robust one. The AB-A model is used to predict the magnetic field along the AB track (Fig. 5a), as well as the field along the MO track (Fig. 5b). The short wavelength signal of the low-altitude measurements is well predicted. Considering the AB-A dataset, rms residuals are 90, 99 and 85 nT for B_r, B_θ and B_ϕ, respectively. Correlation coefficients are 0.95, 0.98 and 0.85. These values are better than those of forward model predictions. This very simple model, based on a spherical source of constant magnetization, explains 75% of the measured signal. This prediction becomes poorer for the high-altitude measurements, with rms residuals of 38, 36 and 31 nT for B_r, B_θ and B_ϕ, respectively, and correlation coefficients of 0.35, 0.89 and 0.88. Only 30% of the signal is explained.

Table 3. Output dipole parameters for AB separated datasets inversion

	Lat. (°N)	**dLat. (°)**	**Lon. (°E)**	**dLon. (°)**	**Depth (km)**	**dDepth (km)**	***m*** **(10^{16} A m^2)**	**dm (10^{16} A m^2)**	***I*** **(°)**	**dI (°)**	***D*** **(°)**	**dD (°)**
Input AB-A	−32.00	1.70	191.00	0.02	50.00	10.00	3.00	2.60	−60.00	1.16	180.00	1.89
AB-A	−31.84	0.02	190.92	0.02	48.94	0.46	3.36	0.09	−49.00	0.03	8.00	0.04
AB-B	−35.20	0.04	199.10	0.02	88.80	0.69	2.70	0.04	−66.00	0.01	−29.00	0.03
AB-C	−33.31	0.02	204.10	0.02	25.56	0.70	1.40	0.07	18.00	0.04	4.00	0.03

dLat., dLon., dDepth, dm, dI and dD are the standard deviations.

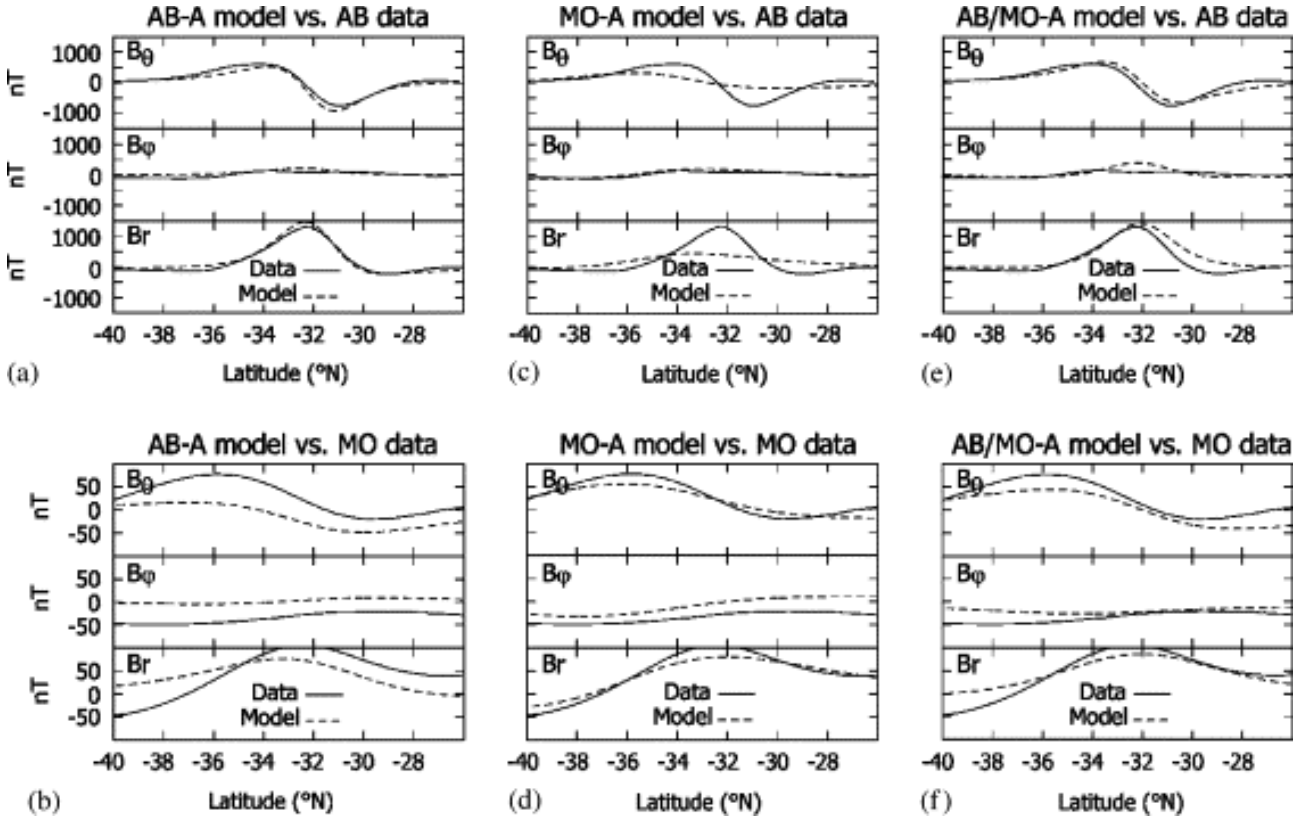

Figure 5: same as Fig. 3 for AB-A dataset inversion model: (a) AB profiles, (b) MO; (c) and (d) for MO-A dataset inversion model; (e) and (f) for AB/MO-A, -B and -C datasets inversion model.

The final latitude of the dipole is 0.2° south of the initial one. It is very well constrained and close to the value given by the forward model. The source of this anomaly is deep in the crust (49 km).

Final parameters for anomalies AB-B and AB-C are also presented in Table 3. The depth of AB-B source is about 89 km, which contrasts with the 25 km depth of the corresponding prism forward model (see Table 2). As expected, its dipolar moment is larger. On the contrary, the source AB-C is closer to the surface (26 km) than the corresponding sphere and prism models. Conversely, its dipolar moment is weaker. Although sources AB-A and AB-B are strongly tilted toward the exterior of the planet, source AB-C is weakly tilted in the opposite direction. However, the three dipoles are nearly pointing to the North.

We then consider together the three AB datasets (628 measurements) to derive the parameters of the three dipoles jointly. Initial SDs do not change with respect to the previous inversion. The solution is stable after one iteration (χ^2=1.25). Output parameters (not shown) are very close to those of the separated cases, except for the AB-B declination.

We finally consider the complete AB dataset (1359 measurements), using similar SDs and input parameters. The resulting χ^2 is larger than previously determined (1.32). This may be due to the fact that some of the measured fields cannot be explained by the three dipoles (e.g. near the northern edge of the area). Final parameters of the three sources do not change significantly (except again for the declination of AB-B source).

The three dipoles (separated case) are used to predict the field at AB and MO measurement

locations. Both the amplitude and lateral extent of the AB anomalies are well represented by the model. For the AB-A dataset, rms residuals are 87, 95 and 61 nT for B_r, B_θ and B_ϕ, respectively, and correlation coefficients are 0.96, 0.98 and 0.86. On the contrary, the model does not fit the MO observations as well as the AB data. Associated rms residuals of MO-A dataset are large (∼30 nT). In particular, the negative features of the northern part of the AB radial map and the one southwestern of the MO radial map are not predicted. The latter one may have a source outside the studied area.

3.3. Inversion of high-altitude data

Second, MO data are considered. We use the same method as for the AB dataset. The two subsets correspond to 17048 and 7886 measurements, respectively (Fig. 2). This large amount of data should enhance the robustness of the solution, despite the lower resolution due to the higher altitude. The input parameters for the dipolar moment are those for the AB-A and AB-C anomalies. Location SDs are set to 100 km. Data SDs are assumed to be 30% of the measurement value, but are never lower than 12 nT. Several initial depths are investigated.

First, the MO-A dataset is considered. The best χ^2 is obtained for a 100 km initial depth. Resulting parameters are indicated in Table 4. The final dipole is located four degrees southwest of the AB-A source. This might explain why the directions are very different from those of AB-A source (the magnetization is almost horizontal). It is also much deeper (154 km instead of 49 km). The field is predicted along a MO track (Fig. 5d). It compares well to the observations: 70% of the signal is explained. For the MO-A dataset, rms residuals are 16, 14 and 17 nT for B_r, B_θ and B_ϕ, respectively. Correlation coefficients are all in excess of 0.9. On the contrary, the AB measurements are not well predicted by this source (Fig. 5c): the depth of the source makes its associated magnetic signature very weak and smooth at low altitude. AB-A dataset rms residuals are large (223, 181 and 61 nT).

Table 4. Output dipole parameters for MO-A, MO-C1 and MO-C2 inversions

	Lat. (°N)	**dLat. (°)**	**Lon. (°E)**	**dLon. (°)**	**Depth (km)**	**dDepth (km)**	***m*** **(10^{16} A m^2)**	**dm (10^{16} A m^2)**	***I*** **(°)**	**dI (°)**	***D*** **(°)**	**dD (°)**
MO-A	−34.77	0.02	187.50	0.02	154.44	0.28	11.01	0.04	−10.30	0.01	39.27	0.01
MO-C1	−31.83	0.02	206.17	0.04	9.03	0.43	1.66	0.01	−17.29	0.01	−36.94	0.01
MO-C2	−32.20	0.04	206.54	0.09	69.82	0.85	2.83	0.01	−20.20	0.01	−39.48	0.01

The MO-C anomaly is also analysed. No significant χ^2 variation with respect to the initial depth is observed. Two sets of parameters are given in Table 4. Despite their very different depth (and dipolar moment), they provide a very similar fit. This suggests that the MO high-altitude dataset alone cannot discriminate depth-to-the-source and dipolar moment.

3.4. Inversion of both AB and MO datasets

We consider the AB/MO-A, AB/MO-B and AB/MO-C sources in a joint inversion of the AB and

MO datasets. The parameters of the three dipoles are solved for, using initial parameters given by the forward modeling. Initial depths are *a priori* set to 50 km for AB/MO-A and -B, and 30 km for AB/MO-C. This reflects the expected better resolution carried by the two altitude datasets. The MO dataset is first decimated to get a similar number of measurements to the AB dataset. MO data SDs are assumed to be 30% of the measurement value, but are never lower than 20 nT. A stable solution is reached after 5 iterations. The distribution of data misfits approaches a gaussian curve. AB-A and MO-A predicted field profiles are shown on Fig. 5e and f, respectively. Correlation coefficients are 0.97, 0.96 and 0.63 for AB B_r, B_θ and B_ϕ profiles, and 0.97, 0.96 and 0.22 for MO. Both AB and MO measurements are well predicted. This simple model for both datasets explains more than 57% of the signal. The parameters of the three dipoles are shown in Table 5. These are close to those of the AB datasets inversion, except for declination values of AB/MO-A (vs. AB-A) and AB/MO-B (vs. AB-B). This is counterbalanced by the steep inclination of these dipoles. Furthermore, all parameters differ strongly with those of MO-A and MO-C. The AB/MO-A dipole is 6 km deeper than the AB-A one and 99 km shallower than the MO-A one. Furthermore AB/MO-A and AB-A locations are similar. This confirms that MO-A source parameters are probably erroneous. AB/MO-B and AB-B source depths are 58 and 89 km, respectively. A weaker magnetization is observed for AB/MO-B source. The same observation can be made on the AB/MO-C depth (31 km), which is comparable to the AB-C one (25 km). This source dipole is also more horizontal than the two others.

Table 5. Output dipole parameters for AB/MO-A, AB/MO-B and AB/MO-C inversions

	Lat. (°N)	**dLat. (°)**	**Lon. (°E)**	**dLon. (°)**	**Depth (km)**	**dDepth (km)**	***m*** **(10^{16} A m^2)**	**dm (10^{16} A m^2)**	***I*** **(°)**	**dI (°)**	***D*** **(°)**	**dD (°)**
AB/MO-A	−32.42	0.02	189.91	0.02	55.29	0.90	3.82	0.01	−56.97	0.02	80.75	0.02
AB/MO-B	−35.33	0.02	198.45	0.02	57.64	0.93	2.58	0.01	−50.73	0.03	53.23	0.01
AB/MO-C	−33.12	0.02	203.59	0.02	31.35	0.95	1.85	0.06	21.08	0.01	12.69	0.02

The three dipoles are used to predict the magnetic field at the measurement locations. We show expected signal at AB and MO locations in Fig. 6. Both the amplitude and the spatial extent of the signal are well described. Similarly to AB only models, differences mostly occur in the radial maps, where the northern and southern negative features associated with the anomaly A are not represented. The rms residuals of the AB-A dataset are 108, 82 and 88 nT for B_r, B_θ and B_ϕ, respectively. Correlation coefficients are 0.94, 0.96 and 0.83. These rms values are a little bit larger than those of the AB-A inversion alone, but much better than those of the MO-A inversion. For MO-A dataset predictions, rms residuals are close to those of the MO-A dataset inversion (∼20 vs. ∼16 nT), and much smaller than those of the AB-A dataset inversion (∼20 vs. ∼35 nT). Correlation coefficients are all in excess of 0.85. These values show that the AB/MO inversion model predicts both AB and MO measurements with large confidence. This demonstrates the complementarity of the two datasets.

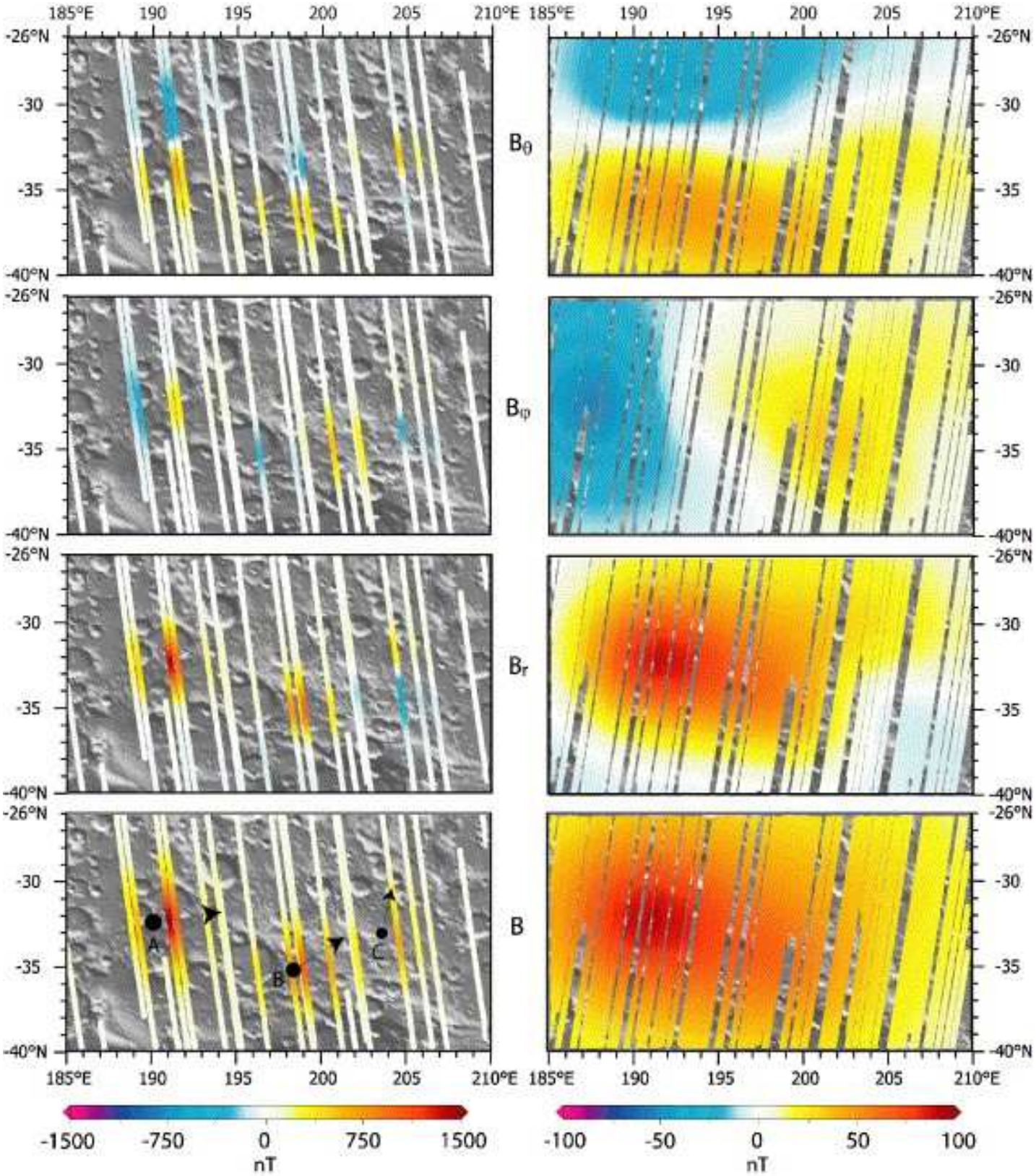

Figure 6: Low- (left) and high- (right) altitude magnetic field created by AB/MO-A, -B and -C inversion models. AB/MO-A, -B and -C dipoles are, respectively, indicated by arrows A, B and C on the AB B component map. The direction of each arrow corresponds with the dipole declination, and the size is proportional to the dipolar moment intensity.

4. Discussion

Assuming a uniformly magnetized sphere tangent to the surface, the AB/MO-A and -B source magnetizations are equal to 54 and 32 A/m, respectively. Using the same approach, AB/MO-C source magnetization would be 143 A/m, for a depth of 31 km. Frawley and Taylor (2004) modeled several anomalies North of our studied area. Their anomaly 4 of area 2 is very close to our anomaly B. The magnetization they derived is on the same order of magnitude (∼20 A/m). The directions are different (−41° vs. −51° for the inclination, and −81° vs. 53° for the declination). In the northern hemisphere, Smrekar et al. (2004) modeled a magnetic anomaly using 6, 9, 12 or 20 A/m magnetized bodies (depending on the inclination). According to Connerney et al. (2001), a body with a 60 A/m magnetization is locally possible. Purucker et al. (2000) found that a 50-km thick layer would have an equivalent magnetization of 20 A/m. Using a similar approach, the equivalent source dipole model of Langlais et al. (2004) predicts a magnetization between ±12 A/m for a 40-km thick layer. Based on spherical harmonic analysis, Arkani-Hamed (2003) concluded that values of 20–30 A/m for the upper 30 km of the crust are required. All these values are very consistent with the AB/MO-A and -B equivalent magnetizations. On the contrary, the AB/MO-C source is much more magnetized. It is also closer to the surface. In addition, its declination and inclination values are very different from those of AB/MO-A and -B sources. This may indicate a different magnetization process.

All these studies (including our results) concur with the fact that the martian crust magnetization is much more intense than the terrestrial one. Fresh oceanic basalts are capable of acquiring a 20 A/m thermo-remanent magnetization (TRM) in a Earth-core field of ∼50000 nT. However, this value decreases rapidly to 5 A/m (Bleil and Petersen, 1983). Another caveat is that the magnetization is often restricted to the upper 2 km of the crust (see Langel and Hinze, 1998, for a review).

Candidate martian magnetic minerals would be magnetite, multi-domain (MD) hematite and single-domain (SD) pyrrhotite. SD pyrrhotite is abundant in martian meteorites (Rochette et al., 2001; Hood et al., 2003), but its Curie temperature (<320 °C) would result in a Curie isotherm too close to the surface. On the contrary, the 675 °C Curie temperature of MD hematite would make it a good candidate for deeper sources. However, its intense thermo-remanent magnetization is not stable with geological time. Christensen et al. (2001) observed superficial hematite deposits. However, they are of small spatial extent (when compared to the magnetic anomalies), and are mainly associated with sedimentary processes. On the Earth, magnetite is the commonest magnetic mineral. Its Curie temperature (580 °C) and its stable remanent magnetization make it the most probable martian magnetic carrier. Assuming a thermal gradient of 10 °C/km in the early martian crust (Choblet and Sotin, 1998), and a surface temperature of 0 °C, then the magnetized layer would be 58 km thick. AB/MO-A and AB/MO-B source depths are very close to this value (55 and 58 km, respectively). On the other hand, the strongly magnetized AB/MO-C dipole is much shallower (31 km). This may suggest that the anomaly was acquired closer to the surface than the two others, maybe at a different time. This can be earlier, at a time when the thermal gradient of the martian crust was higher. This may also indicate that the magnetic minerals were more abundant or that the dynamic magnetic field was stronger.

There have been several estimates for the crustal thickness. Voorhies et al. (2002) gave a value to 50 km, based on the magnetic power spectrum of the magnetic anomalies. Zuber (2001) estimated the mean thickness of the martian crust to be 50 km, using a specific model (2900 and 3500 kg/m^3 for crust and mantle density, respectively). This is a mean value and it is much more thick under the craterized highlands in the South hemisphere. Assuming a mean value of 2 km for the elevation of the topography inside our area, the associated crustal root is 10 km. The corresponding thickness is then 62 km. Based on geochemical data from SNC meteorites and on polar moment of inertia

factor, Sohl and Spohn (1997) found that the crustal thickness ranges between 110 and 250 km.

On the Earth, both primary and secondary magnetite can bear strong magnetizations. TRM processes are the main sources for crustal magnetization. Primary magnetite minerals inside fresh oceanic basalts acquire their magnetization while cooling in the Earth's core magnetic field. Chemical remanent magnetization (CRM) processes are another possibility. Secondary magnetite can result from a serpentinization process (Nazarova, 1994):

$$30\left(Mg_{0.8}Fe_{0.2}\right)SiO_3 + 18\,H_2O \rightarrow 8\,Mg_2Si_2O_5\left(OH\right)_4 + 2\,Fe_3O_4 + 2\,H_2 + 14\,SiO_2$$

Enstatite (20 % Fe) + Water → Lizardite + Magnetite + Dihydrogen + Quartz

This reaction shows that a 8% hydration of a basaltic crust composed of enstatite produces a 10% volume-fraction of magnetite. According to Toft et al. (1990) the resulting magnetic susceptibility would be 0.32 SI. Under an Earth-like magnetic field (~50,000 nT), the corresponding induced magnetization would be 12.7 A/m. Assuming a Koenigsberger ratio between 1 and 10 (Gopala Rao and Krishna, 2002), the remanent magnetization would range between 12.7 and 127 A/m. Such high values could explain the intense martian magnetic anomalies.

This serpentinization scenario relies on a hydrated crust, a mantle convection (to heat the crust) and a core field early in the history of Mars. It has long been recognized that water was present on early Mars (Carr, 1996; Hauck and Phillips, 2002; Solomon et al., 2005). The lack of magnetic signal over Hellas and Argyre (3.9 Ga) giant impact craters reveals that no magnetic field occurred during the post-impact crustal cooling. This indicates that the core field turned off before (Acuña et al., 1999) or, that it started after these impacts (Schubert et al., 2000). However, the major part of the magnetized surface is Noachian. Furthermore, numerical models show that both mantle convection and a dynamo were likely to occur during the first 500 Myr of Mars (Breuer and Spohn, 2003). This favors the hypothesis of an early core field.

In the following we investigate the possible evolution of the martian dynamo. This is done by deriving virtual magnetic paleopoles associated with our three anomalies. Considering AB/MO-A, AB/MO-B and AB/MO-C sources, paleopoles are located at (25.7°N, 309.6°E), (45.9°N, 299.2°E) and (44.3°N, 221.1°E), respectively. Since the final variance on both declination and inclination are small (Table 5), the formal standard deviation on these locations is less than 1°. These three poles are close to the Tharsis bulge edges (Fig. 7). These values are compared to those of previous studies. The paleopole associated with anomaly 4 of Frawley and Taylor (2004) is found at (20°N, 90°E). This does not correlate with our paleopoles. Arkani-Hamed and Boutin (2004) derived paleopole positions from nine isolated magnetic anomalies. Six out of 9 of these paleopoles clustered around (20°N, 260°E). Hood and Zakharian (2001) used low-altitude measurements to determine the characteristics of two northern hemisphere anomalies. Associated paleopoles were found at (61°N, 230°E) and (38°N, 220°E). All these studies concur to middle latitudes for the paleopoles. On the contrary, Langlais and Purucker (2006) found a paleopole at (88°N, 279°E) very close to the present day rotation axis. Assuming that the Tharsis dome's emplacement occurred before Apollinaris Patera acquired its magnetic signature, these results may be reconciled if Tharsis formed at higher latitudes, inducing a major polar wander resulting in its displacement toward its present location (Melosh, 1980; Sprenke and Baker, 2000; Hood and Zakharian, 2001).

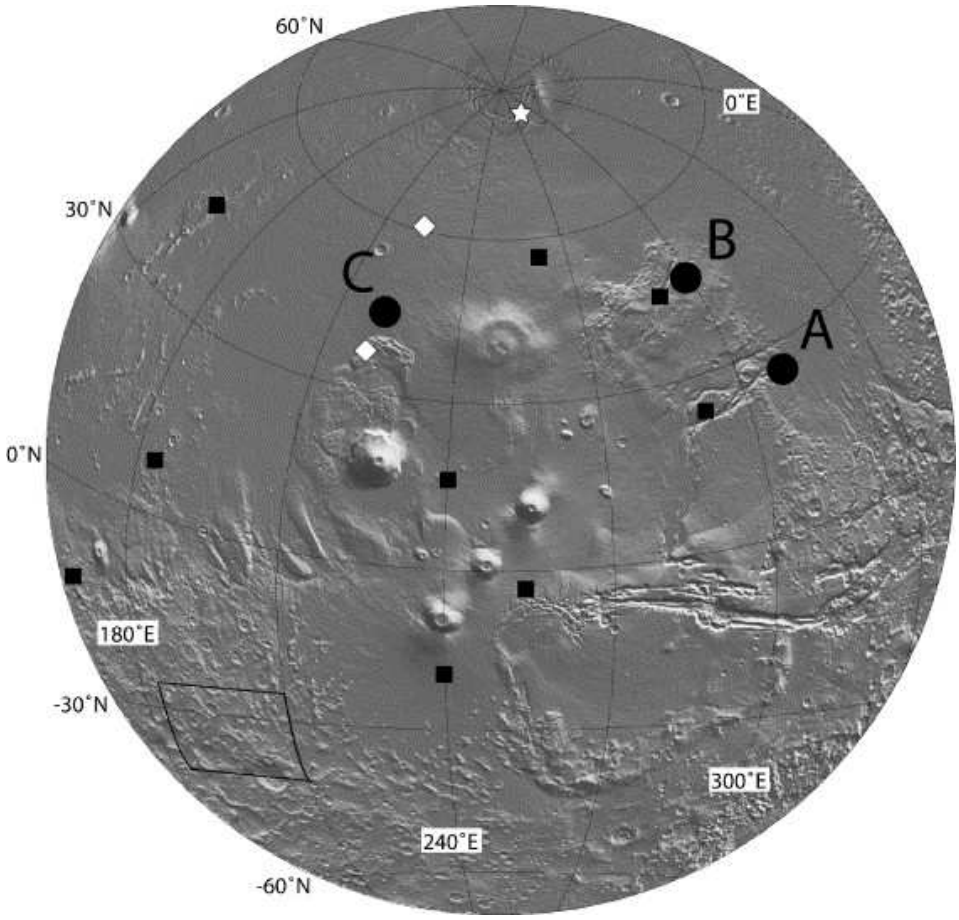

Figure 7: Locations of the AB/MO-A, -B and -C paleopoles over a hemispheric gray-shaded map of Mars. Black squares represent paleopoles found by Arkani-Hamed and Boutin (2004). White diamonds correspond with the two paleopoles derived by Hood and Zakharian (2001). The white star is the paleopole derived by Langlais and Purucker (2006). The solid line in black limits the studied area.

However, the absence of coherence between the three paleopoles derived here have to be explained. Paleopole determination relies on the basic assumption that the core field was axial dipolar (Butler, 1992), which may be erroneous. Also, contiguous areas could originate from different regions, as it is observed on the Earth. But such displacements would result in tectonic signatures, that are not visible. One has also to consider the possible evolution of the magnetic properties since they were put into place. Demagnetization processes, such as impacts, may have occurred. Large impact craters are not associated with magnetic signatures (Acuña et al., 1999). Smaller craters may induce partial demagnetization (Melosh, 1989), that would result in non-uniform magnetization. Our AB/MO-A anomaly lies to the southwest of a 100 km-diameter crater. But this crater is probably too small to demagnetize more than 10 km of crust. Another possibility is the relative timing of magnetic anomalies. Their magnetization may have been acquired under a different global martian magnetic field.

It will be very difficult to discriminate between all these hypotheses until new measurements are made available. Low-altitude measurements, either on low-periapsis spacecraft, or airborne surveys, are crucially needed.

5. Conclusion

In this study, we characterize three martian magnetic anomalies over a Terra Sirenum local area. Low- and high-altitude measurements are taken into account. We first use simple forward models such as spheres and prisms to fit the signal. Then, a generalized non-linear inversion is applied to the different datasets. Finally, we use the two datasets together. A non-linear scheme is used to determine every one of the six dipole parameters (location and magnetization components). Low-altitude measurements can be used to characterize local (and shallow) magnetic sources. On the contrary, inversion of high-altitude data alone is not recommended to study isolated martian magnetic sources. Nevertheless, we demonstrate that the two datasets are complementary. AB measurements strongly constrain depth and dipolar moment of sources, whereas MO data give further information on the regional context.

Our forward and inverse models reveal that two low-altitude martian magnetic anomalies in Terra Sirenum (AB-A and AB-B) are caused by large amplitude intensity magnetic sources located deep in the crust (>40 km). However, shallower sources can exist (AB/MO-C). Finally, we show that nearby crustal magnetic sources can have different characteristics.

These results imply different origins or other post-magnetization processes. We propose that serpentinization of the early martian crust can produce such magnetic anomalies, in the presence of water, a core dynamo and mantle convection. By studying Mars' magnetic field, and by comparing it with those of other planets, we will improve our knowledge on the mechanisms that allow an iron-rich liquid core to generate a self-sustained dynamo. Low-altitude magnetic measurements are essential to characterize the ancient martian magnetic field. A new mission with very low-altitude magnetic measurements is crucial. Especially, our magnetic sources depths (∼50 km) must be confirmed by future aero- or ground magnetic surveys.

Acknowledgements
This work benefited from the support of the European Community's Improving Human Potential Programme under contract RTN2-2001-00414, MAGE. This study was also supported by INSU/CNES Programme National de Planétologie. We thank the MAG-ER team for the MGS magnetic data, M. Purucker for constructive discussions and the anonymous reviewer for helpful comments and suggestions.

References

Acuna, M.H., Connerney, J.E.P., Ness, N.F., Lin, R.P., Mitchell, D., Carlson, C.W., McFadden, J., Anderson, K.A., Re`me, H., Mazelle, C., Vignes, D., Wasilewski, P., Cloutier, P., 1999. Global distribution of crustal magnetization discovered by the Mars Global Surveyor MAG/ER experiment. Science 284, 790–793.

Arkani-Hamed, J., 2001. A 50-degree spherical harmonic model of the magnetic field of Mars. J. Geophys. Res. 106 (E10), 23197–23208.

Arkani-Hamed, J., 2003. Thermoremanent magnetization of the Martian lithosphere. J. Geophys. Res. 108 (E10), 5114, 3–4.

Arkani-Hamed, J., 2004. A coherent model of the crustal magnetic field of Mars. J. Geophys. Res. 109, E09005.

Arkani-Hamed, J., Boutin, D., 2004. Paleomagnetic poles of Mars: revisited. J. Geophys. Res. 109, E03011.

Blakely, R.J., 1995. Potential Theory in Gravity and Magnetic Applications. Cambridge University Press, Cambridge, (441 pp).

Bleil, U., Petersen, N., 1983. Variations in magnetization intensity and low-temperature titanomagnetite oxidation of ocean floor basalts. Nature 301, 384–388.

Breuer, D., Spohn, T., 2003. Early plate tectonics versus single-plate tectonics on Mars: evidence from magnetic field history and crust evolution. J. Geophys. Res. (Planets) 108 (E7), 5072.

Butler, R.F., 1992. Paleomagnetism: Magnetic Domains to Geologic Terranes. Blackwell Sci., Malden, MA, (319pp).

Cain, J.C., Ferguson, B.B., Mazzoni, D., 2003. An n=90 internal potential function of the Martian crustal magnetic field. J. Geophys. Res. 108 (E2), 5008.

Carr, M., 1996. Water on Mars. Oxford University Press, New York, (248pp).

Choblet, G., Sotin, C., 1998. Early transient cooling of Mars. Geophys. Res. Lett. 28 (15), 3035–3038.

Christensen, P.R., Morris, R.V., Lane, M.D., Bandfield, J.L., Malin, M.C., 2001. Global mapping of Martian hematite mineral deposits: remnants of water-driven processes on early Mars. J. Geophys. Res. 106 (E10), 23873–23885.

Connerney, J.E.P., Acuna, M.H., Wasilewski, P.J., Kletetschka, G., Ness, N.F., Rème, H., Lin, R.P., Mitchell, D.L., 2001. The global magnetic field of mars and implications for crustal evolution. Geophys. Res. Lett. 28, 4015–4018.

Frawley, J.J., Taylor, P.T., 2004. Paleo-pole positions from martian magnetic anomaly data. Icarus 172, 316–327.

Gopala Rao, D., Krishna, K.S., 2002. Magnetic rock properties of the gabbros from the ODP Drill Hole 1105A of the Atlantis Bank, Southwest Indian Ridge. Proc. Indian Acad. Sci. (Earth Planet. Sci.) 111 (4), 467–481.

Harrison, K.P., Grimm, R.E., 2002. Controls on martian hydrothermal systems: application to valley network and magnetic anomaly formation. J. Geophys. Res. 107 (E5), 5025.

Hartmann, W.K., Neukum, G., 2001. Cratering chronology and the evolution of Mars. Space Sci. Rev. 96, 165–194.

Hauck II, S.A., Phillips, R.J., 2002. Thermal and crustal evolution of Mars. J. Geophys. Res. 107 (E7), 5052.

Hood, L.L., Zakharian, A., 2001. Mapping and modeling of magnetic anomalies in the northern polar region of Mars. J. Geophys. Res. 106, 14601–14620.

Hood, L.L., Richmond, N.C., Pierazzo, E., Rochette, P., 2003. Distribution of crustal magnetic fields on mars: shock effects of basin-forming impacts. Geophys. Res. Lett. 30 (6), 1281.

Hood, L.L., Young, C.N., Richmond, N.C., Harrison, K.P., 2005. Modeling of major martian magnetic anomalies: further evidence for polar reorientations during the Noachian. Icarus 177 (1), 144–173.

Jakosky, B.M., Phillips, R.J., 2001. Mars' volatile and climate history. Nature 412, 237–244.

Langel, R.A., Hinze, W.J., 1998. The Magnetic Field of the Earth's Lithosphere: The Satellite Perspective. Cambridge University Press, Cambridge.

Langlais, B., Purucker, M.E., 2006. A polar magnetic paleopole associated with Apollinaris Patera, Mars. Planet. Sp. Sci., this issue.

Langlais, B., Purucker, M.E., Mandea, M., 2004. Crustal magnetic field of Mars. J. Geophys. Res. 109, E02008.

Melosh, H.J., 1980. Tectonic patterns on a reoriented planet. Icarus 44, 745–751.

Melosh, H.J., 1989. Impact Cratering: A Geologic Process. Oxford University Press, New York, (245pp).

Nazarova, K.A., 1994. Serpentinized peridotites as a possible source for oceanic magnetic anomalies. Marine Geophysical Researches 16, 455–462.

Plouff, D., 1976. Gravity and magnetic fields of polygonal prisms and application to magnetic terrain corrections. Geophysics 41 (4), 727–741.

Purucker, M., Ravat, D., Frey, H., Voorhies, C., Sabaka, T., Acun˜ a, M., 2000. An altitude-normalized magnetic map of Mars and its interpretation. Geophys. Res. Lett. 27 (16), 2449–2452.

Rochette, P., Lorand, J.-P., Fillion, G., Sautter, V., 2001. Pyrrhotite and the remanent magnetization of SNC meteorites: a changing perspective on Martian magnetism. Earth Planet. Sci. Lett. 190, 1–12.

Schubert, G., Russell, C.T., Moore, W.B., 2000. Timing of the Martian dynamo. Nature 408, 666–667.

Scott, E.R.D., Fuller, M., 2004. A possible source for the Martian crustal magnetic field. Earth Planet. Sci. Lett. 220, 83–90.

Smrekar, S.E., McGill, G.E., Raymond, C.A., Dimitriou, A.M., 2004. Geologic Evolution of the Martian dichotomy in the Ismenius area of Mars and implications for plains magnetization. J. Geophys. Res. 109, E11002.

Sohl, F., Spohn, T., 1997. The interior structure of Mars: implications from SNC meteorites. J. Geophys. Res. 102 (E1), 1613–1635.

Solomon, S.C., Aharonson, O., Aurnou, J.M., Banerdt, W.B., Carr, M.H., Dombard, A.J., Frey, H.V.,

Golombek, M.P., Hauck II, S.A., Head III, J.W., Jakosky, B.M., Johnson, C.L., McGovern, P.J., Neumann, G.A., Phillips, R.J., Smith, D.E., Zuber, M.T., 2005. New perspectives on ancient Mars. Science 307, 1214–1220.

Sprenke, K.F., Baker, L.L., 2000. Magnetization, paleomagnetic poles, and polar wander on Mars. Icarus 147, 26–34.

Talwani, M., 1965. Computation with the help of a digital computer of magnetic anomalies caused by bodies of arbitrary shape. Geophysics 30 (5), 797–817.

Tanaka, K.L., 1986. The stratigraphy of Mars. J. Geophys. Res. 91 (B13), E139–E158.

Tarantola, A., Valette, B., 1982. Generalized non-linear inverse problems solved using the least-squares criterion. Rev. Geophys. Space Phys. 20(2), 219–232.

Toft, P.B., Arkani-Hamed, J., Haggerty, S.E., 1990. The effects of serpentinization on density and magnetic susceptibility: a petrophysical model. Phys. Earth Planet. Inter. 65, 137–157.

Voorhies, C.V., Sabaka, T.J., Purucker, M., 2002. On magnetic spectra of Earth and Mars. J. Geophys. Res. 107, 1.1–1.11.

Wilson, L., Head, J.W., 2002. Tharsis-radial graben systems as the surface manifestation of plume-related dike intrusion complexes: models and implications. J. Geophys. Res. 107 (E8).

Yuan, D.N., Sjogren, W.L., Konopliv, A.S., Kucinskas, A.B., 2001. Gravity field of Mars: a 75th degree and order model. J. Geophys. Res. 106 (E10), 23377–23401.

Zuber, M.T., 2001. The crust and the mantle of Mars. Nature 412, 220–227.